Journal of Materials Chemistry A

ROYAL SOCIETY OF CHEMISTRY

PAPER

View Article Online
View Journal | View Issue

Cite this: J. Mater. Chem. A, 2023, 11, 25410

Reaction mechanism and kinetics of oxygen reduction reaction on the iron–nickel dual atom catalyst†

Mohsen Tamtaji, [a] Yuyin Li, [b] Yuting Cai,[b] Hongwei Liu,[b] William A. Goddard III *[c] and GuanHua Chen*[ad]

Dual-atom catalysts (DACs) have recently emerged as promising and high-activity catalysts for the oxygen reduction reaction (ORR), a key process in many electrochemical energy conversion devices. However, the ORR mechanism and kinetics on DACs has not yet been established. To address this problem, we employed grand canonical potential kinetics (GCP-K) with CANDLE solvation. The behavior of the free energy and grand canonical potential for ORR and hydrogen evolution reaction (HER) intermediates (OO*, OOH*, O*, OH*, and H*) and their corresponding transition states at constant charges were calculated and converted to free energy as a function of applied potential to predict current density as a function of applied potential for ORR (through the associative pathway) and the competitive HER on iron–nickel DAC (FeNiN6-DAC). We find a Tafel slope of 281 mV dec^{-1} for ORR, comparable with the experimental Tafel slope of 169 mV dec^{-1} at the current density of −1.7 mA cm^{-2}. The change in concentration of ORR reaction intermediates on FeNiN6-DAC as a function of applied potentials indicates that the dominant intermediate is OH* at potentials >0.25 V *vs.* RHE. The charge transfer and spin density of Fe active sites reaches a maximum during each proton transfer step. The partial density of states of 3d orbitals on the Fe site indicates that the $3d_{x^2-y^2}$ orbital is near the Fermi level, while the position of the $3d_{z^2}$ orbital and Fermi level reaches a minimum along the first reaction step of OO* $\xrightarrow{H^+}$ OOH*. These insights into the fundamental aspects of ORR on DACs provide guidance for the design of efficient catalysts.

Received 20th September 2023
Accepted 16th October 2023

DOI: 10.1039/d3ta05694e

rsc.li/materials-a

1. Introduction

Efficient oxygen reduction reaction (ORR) to ensure rapid reaction kinetics is a crucial process in many electrochemical energy conversion devices, including fuel cells, metal–air batteries, and electrolyzers.[1,2] In ORR, the dioxygen is reduced through the OOH*, O*, and OH* reaction intermediates to produce two water molecules *via* the four-electron transfer pathway and/or a H_2O_2 molecule *via* a two-electron transfer pathway, as shown in Scheme 1,[3–5] typically occurring at the cathode of these devices. However, a major bottleneck for the commercialization of catalysts is the sluggish kinetics and the competition with the hydrogen evolution reaction (HER) as shown in Scheme 1.[6,7] Therefore, to develop new catalysts with high efficiency and rapid reaction kinetics toward ORR, there is an urgent need to investigate the fundamentals behind their reaction mechanism.

Dual atom catalysts (DACs) have recently attracted widespread interest towards high-performance electrochemical reactions by enabling regulation of the electronic structure and spin state of the metal centers.[8–13] Thus, co-doping a counterpart metal beside the active metal site can act as electron donors to help stabilize the intermediate species in the reaction mechanism.[14–16] Previous studies have applied theoretical calculations and experimental synthesis to DACs for various electrochemical applications such as CO_2 reduction reaction (CO_2RR), nitrogen reduction reaction (NRR), HER, and ORR.[17–24] The theoretical studies for ORR have mainly reported the Gibbs free energy (ΔG) of the main reaction intermediates such as H*, OH*, O*, OOH*, and OO* at zero net charge with the goal of predicting the limiting potential (φ) and overpotential ($\eta = 1.23 - \varphi$).[25–27] In most calculations, the dependence of the Gibbs free energy of the intermediates is assumed to be linear in the applied potential (U) as:

[a]Hong Kong Quantum AI Lab Limited, Pak Shek Kok, Hong Kong SAR, China
[b]Department of Chemical and Biological Engineering, Guangdong-Hong Kong-Macao Joint Laboratory for Intelligent Micro-Nano Optoelectronic Technology, William Mong Institute of Nano Science and Technology, Hong Kong Branch of Chinese National Engineering Research Center for Tissue Restoration and Reconstruction, The Hong Kong University of Science and Technology, Clear Water Bay, Kowloon, Hong Kong, 999077, P. R. China
[c]Materials and Process Simulation Center (MSC), California Institute of Technology, MC 139-74, Pasadena, CA, 91125, USA. E-mail: wag@caltech.edu
[d]Department of Chemistry, The University of Hong Kong, Pokfulam Road, Hong Kong SAR, China. E-mail: ghc@everest.hku.hk

† Electronic supplementary information (ESI) available: Grand canonical potential kinetics and density of states. See DOI: https://doi.org/10.1039/d3ta05694e

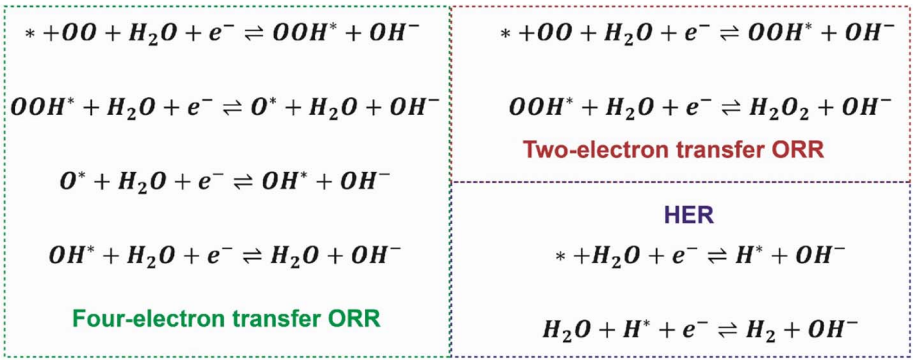

Scheme 1 Reaction steps. Reaction steps of four- and two-electron transfer oxygen reduction reaction (ORR) and hydrogen evolution reaction (HER).

$$\Delta G_{OH*}(U) = \Delta G_{OH*}|_{at\ U=0\ V} - eU \quad (1)$$

$$\Delta G_{O*}(U) = \Delta G_{O*}|_{at\ U=0\ V} - 2eU \quad (2)$$

$$\Delta G_{OOH*}(U) = \Delta G_{OOH*}|_{at\ U=0\ V} - 3eU \quad (3)$$

where e is the electron charge.[28–30] However, linear dependence is assumed and has been shown to be incorrect in some studies.[31,32] In addition, the zero-potential Gibbs free energies are generally assumed to be equal to the zero-charge values and the potential of zero charge (U_{PZC}) at which the system is neutral is assumed to be 0 V. However, it has been shown that the potential of zero charge at neutral charges is higher than 0, and at zero potential, the intermediates are not neutral.[33] Importantly, the transition states between the OO*, OOH*, O*, OH*, and H* intermediates are essential to provide an understanding of the ORR reaction mechanism and kinetics on DACs. That is, we need to calculate the reaction barriers, reaction rates, charge transfer, and spin population of active metal site along the proton transfer steps that give rise to the current–potential (I–V) curves, Tafel slopes, and the concentration of each reaction intermediate on the catalyst's surface.[34–36]

In addition, investigation of partial density of states along the proton transfer steps is needed to understand the changes in molecular orbital configurations responsible for the evolution in bonding interactions and Gibbs free energies. These aspects have been investigated partially for several electrochemical reactions on various catalysts. For example, the reaction mechanism and kinetics of CO_2 reduction to CO on nickel single atom catalyst (SAC) was examined, indicating that the rate-determining step is the proton transfer to CO_2.[33] In addition, the mechanism and predicted kinetics as a function of applied potential for NRR and HER for the iron–ruthenium DAC was reported, leading to the onset potential of −0.22 V *vs.* Reversible Hydrogen Electrode (RHE) at the current density of 10 mA cm^{-2} for ammonia synthesis.[32]

In this work, we employ DFT calculations to examine ORR and HER mechanisms on the iron–nickel DAC (FeNiN6-DAC). We use VASPsol code to perform structural relaxation for OO*, OOH*, O*, OH*, and H* intermediates, and the climbing image nudged elastic band (CI-NEB) calculation for calculating transition states between the reaction intermediates. Then we used the joint DFT calculations with CANDLE solvation to calculate the free energy of reaction intermediates and transition states at constant charges ($n - n_0 = 0$, 0.5, 1, and 1.5 e$^-$). Applying a Legendre transformation, converts the constant-charge free energies to constant-potential free energies which was used to calculate reaction rates as a function of applied potential. The behavior of free energy, grand canonical potential, charge transfer, spin population, and density of states of Fe metal was investigated along the reaction pathway. The resulting I–V curve and Tafel slopes for ORR and HER were calculated and compared with experimental results in the literature. The change in the concentration of ORR reaction intermediates on the Fe active site of FeNiN6-DAC indicates that at high potentials, the proton transfer to OH* to producer water is the rate limiting step, while at low potentials, the proton transfer to O* to producer OH* is the rate limiting step.

2. Grand canonical potential kinetics formulation

2.1 Structural relaxation and free energy calculations

In this study, we used a combination of spin-polarized DFT calculations and solvation models to investigate ORR mechanism on the FeNiN6-DAC. The calculations were performed using the Vienna *Ab initio* Simulation Package (VASP, version 5.4.4) and jDFTx (version 1.7.0) software. The relaxed structure of the reaction intermediates were calculated using the VASPsol solvation code in VASP at constant charge using the Perdew–Burke–Ernzerhof (PBE) functional. The climbing image nudged elastic band (CI-NEB) method was then employed in the VTST package to obtain the relaxed structure of transition states as a function of net charges ($n - n_0$) using VASPsol solvation code. The DFT-D3 method was used to account for London dispersion (van der Waals attraction) interactions.[37] To describe the explicit polarization effect involved in proton transfer events, we added three explicit water molecules in a vertical direction to the reaction system and performed the structural relaxation in VASPsol with a default dielectric constant of $\varepsilon = 78.4$ for water.[32–34] It is worth mentioning that introducing only three

explicit water molecules into the systems in the vertical direction, might not fully describe the influence of the dynamic hydrogen bond network and might have some impacts on the calculated reaction barriers. In fact, the hydrogen dynamic transfer can also happen between more than three water molecules in other directions. As shown in Fig. 1a, a 4×4 supercell of graphene was constructed (12.8 Å $\times$ 12.8 Å), and an iron–nickel pair was placed at the four carbon vacancies and coordinated with six nitrogen atoms (FeNiN6-DAC). A 20 Å vacuum space was added along the z direction to avoid any interaction between periodic images, the Brillouin zone was sampled by the $4 \times 4 \times 1$ Monkhorst–Pack k-point scheme, and the energy cutoff was set at 500 eV. The convergence criteria were set as 10^{-6} eV in energy and 0.02 eV Å^{-1} in force for the structure relation of intermediates while the convergence criteria were set as 10^{-8} eV in energy and 0.05 eV Å^{-1} in force for CI-NEB calculations for the structure relation of transition states.

To obtain the single-point free energy of reaction intermediates and their corresponding transition states, the VASP-optimized stagnation points at a series of constant charges were calculated in jDFTx. The constant-charge free energy was then transformed to constant-potential free energy through the Legendre transformation. The CANDLE solvation model was used for all single-point free energy calculations with chemical potential of an electron ($\mu_{e,SHE} = 4.66$ eV) at the standard hydrogen electrode (SHE). The reference Fermi energy of the electron was corrected by 0.0592 $\times$ pH. All the single-point free energy calculations used a plane wave basis set with a $4 \times 4 \times 1$ k-point mesh and energy cutoff of 20 hartree, and the free energy convergence was set to the default 10^{-8} hartree.

2.2 Legendre transformation

Our recently developed GCP-K methodology can be used to determine the kinetics for heterogeneous electrochemistry as a function of net charges and applied potential while allowing the transition states to evolve continuously.[33] GCP-K uses a Legendre transformation to convert the fixed-charge single-point free energy in jDFTx code, $F(n)$, to grand canonical free energy, $G(n;U)$, allowing the thermodynamic free energy for heterogeneous electrochemical reactions to depend on the

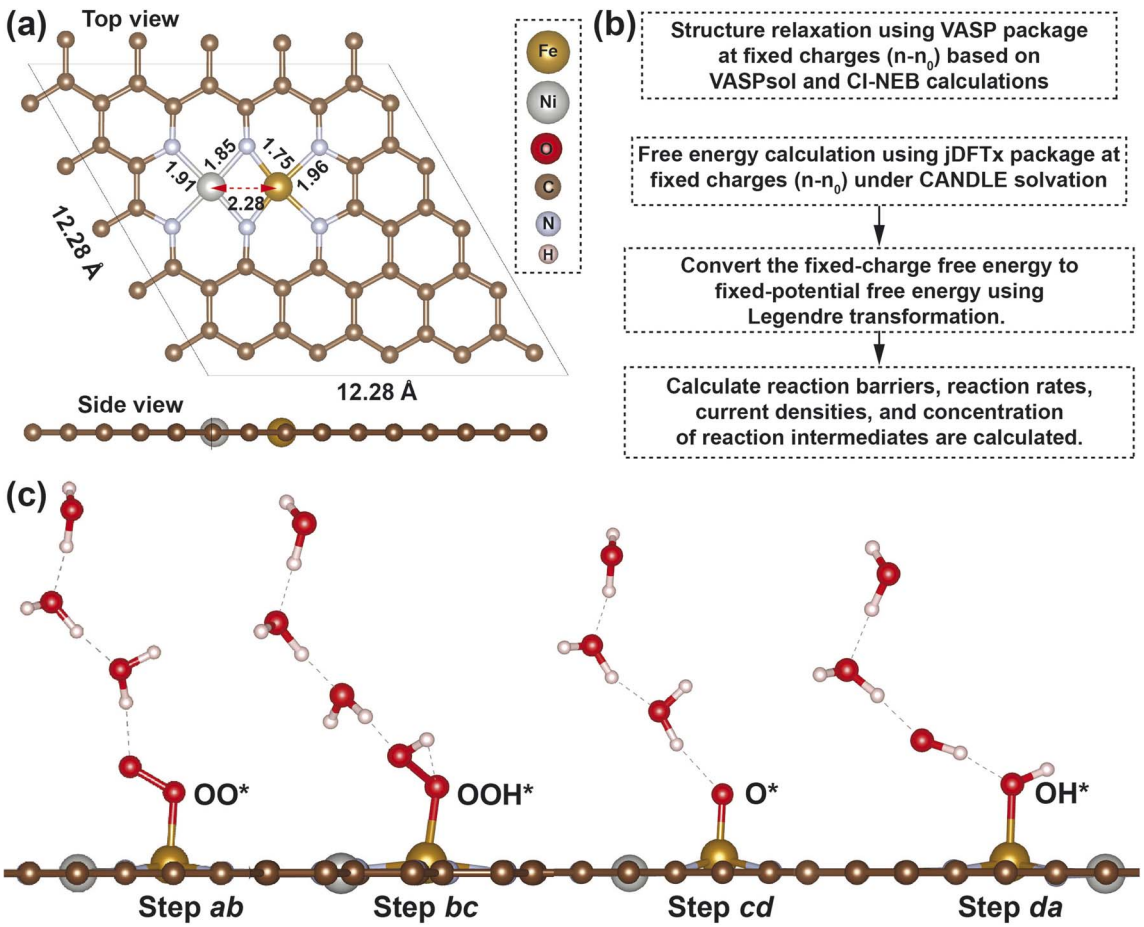

Fig. 1 Oxygen reduction reaction (ORR) mechanism on FeNiN6-DAC. (a) Top and side view of the optimized structure model of FeNiN6-DAC (dark gray color balls: carbon, gray color ball: iron, light blue color balls: nitrogen, red color balls: oxygen, salmon color balls: hydrogen, and cream color ball: nickel). Fe and Ni are anchored on the moiety side and the bond lengths are in Å. (b) The overall calculation procedure of the GCP-K method. (c) Graphical description of the ORR pathway catalyzed by FeNiN6-DAC at the applied potential of 1 V *vs.* RHE.

applied potential (U). The derivation starts with the general definition of the grand canonical potential:[38]

$$G(n;U) = F(n) - ne(U_{SHE} - U) \quad (4)$$

where G is the grand canonical free energy, which depends on the number of electrons (n), the applied potential (U *vs.* SHE), and the total free energy ($F(n)$). The sign of U is defined as the potential used in experiments, *i.e.*, $U = -0.7$ V corresponds to -0.7 V *vs.* SHE. We calculate how the number of electrons depends on the applied potential to obtain $G(n;U)$ as a thermodynamic potential. To do this, we shift the Fermi level to correspond to the applied potential by changing the electronic band occupation, varying the number of electrons in the systems (eqn (4)). Finally, we obtain grand canonical potential (GCP(U)) through minimizing $G(n;U)$ according to ref. 38:

$$\frac{dG(n;U)}{dn} = 0 \text{ or } \mu_{e,SHE} = \frac{dF(n)}{dn} = e(U_{SHE} - U) \quad (5)$$

Minimizing $G(n;U)$ leads to a quadratic form in GCP(U). To obtain GCP(U) we fit a quadratic expansion of $F(n)$:[33]

$$F(n) = a(n - n_0)^2 + b(n - n_0) + c \quad (6)$$

where a, b, and c ($=F(n = n_0)$) are determined from fitting. So, the grand canonical potential is as follows:[39]

$$G(n;U) = a(n - n_0)^2 + (b - (U_{SHE} - U))(n - n_0) + c + n_0e(U_{SHE} - U) \quad (7)$$

Minimization of grand canonical potential leads to ref. 39:

$$GCP(U) = -\frac{1}{4a}(b - \mu_{e,SHE} + eU)^2 + c - n_0\mu_{e,SHE} + n_0eU \quad (8)$$

The parameter a is related to the differential capacitance, $C_{diff} = \frac{\partial n}{\partial U} = -\frac{1}{2a}$, while the parameter b is related to the potential of zero charge, $U_{PZC} = b/e - \mu_{e,SHE}/e$. Since at the potential of zero charge, the system is neutral, $n(U_{PZC}) = n_0$, we can write $U - U_{PZC} = \frac{1}{C_{diff}}(n - n_0)$. So:[39]

$$n(U) = -\frac{1}{e}\frac{\partial GCP(U)}{\partial U} = n_0 - \frac{1}{2ae}(b - \mu_{e,SHE} + eU_{PZC}) \quad (9)$$

Thus, we can write, $b = \mu_{e,SHE} - eU_{PZC}$. Putting these physical quantities into eqn (4) and (5), we write the free energy and grand canonical potential as follows:[39]

$$F(n) = -\frac{1}{2C_{diff}}(n - n_0)^2 + (\mu_{e,SHE} - eU)(n - n_0) + F_0 \quad (10)$$

$$GCP(U) = -\frac{e^2C_{diff}}{2}(U - U_{PZC})^2 + n_0eU + F_0 - n_0\mu_{e,SHE} \quad (11)$$

where, n_0 is the number of electrons at zero net charge (total number of valence electron) and $\mu_{e,SHE}$ is the chemical potential of an electron *vs.* SHE. This quadratic form of free energy $F(n)$ and grand canonical potential GCP(U) accounts for the change in capacitance as the potential changes.[33]

3. Results and discussion

We have investigated the reaction mechanism of oxygen reduction reaction (ORR) in both four-electron transfer pathway and the two-electron transfer pathway along with the competitive HER on FeNiN6-DAC which the reaction steps are shown in Scheme 1. Fig. 1a shows top and side view of the optimized structure model of FeNiN6-DAC. Fe and Ni are anchored on the moiety side and the bond lengths are denoted in Å. As shown in Fig. 1b, we used DFT calculations in the VASP package for structure relaxation of the intermediates and the CI-NEB calculations for structure relaxation of transition states at constant charges ($n - n_0 = 0$, 0.5, 1, and 1.5 e^-). Then, we used single point calculations in jDFTx package to calculate constant-charge free energies under CANDLE solvation. The Legendre transformation was then used to convert the fixed-charge free energies to the fixed-potential free energies and to convert the free energy ($F(n)$) to grand canonical potential (GCP(U)) and reaction barriers. Next, reaction rates, current densities, and concentration of reaction intermediates were calculated.

As shown in Fig. S1,† adsorption of dioxygen which is the first step of ORR on FeNiN6-DAC can be *via* either end-on or side-on orientation and can lead to either associative or enzymatic pathways, respectively. As shown in Fig. S2,† the calculated adsorption free energy of dioxygen at the potential of zero charge ($U = U_{PZC}$ and $n = n_0$) is -0.85 eV lower for the end-on configuration and because it is not an electrochemical step, the effect of applied potential is assumed to be negligible on the O_2 adsorption. This indicates that end-on configuration (associative pathway) on FeNiN6-DAC is far more favorable than side-on configuration (enzymatic pathway) for all the potentials. This also indicates that Fe acts as an active metal center and Ni acts only as the electron donor providing electronic modulation to the Fe site, in agreement with previous reports.[14] This can be explained by the fact that the adsorption of dioxygen on Ni single atom site is very weak compared to Fe site.[40] When the O_2 binds *via* the end-on configuration, the O–O bond elongates from its nominal value of 1.24 Å to 1.29 Å. Fig. 1c indicates graphical description of the ORR intermediates in which three explicit water molecules was added to the reaction system to describe the explicit polarization effect involved in proton transfers.

The geometry and free energy level of six transition states was investigated between each intermediate steps of ab ($OO^* \xrightarrow{H^+} OOH^*$), bc ($OOH^* \xrightarrow{H^+} O^* + H_2O$), cd ($O^* \xrightarrow{H^+} OH^*$), da ($OH^* \xrightarrow{H^+} H_2O$), ae ($^* \xrightarrow{H^+} H^*$), and ef ($H^* \xrightarrow{H^+} H_2$). Then, we considered the behavior of the free energy and grand canonical potential as a function of the number of electrons for each reaction intermediate and their corresponding transition states. For example, Fig. 2a demonstrates the free energies ($F(n)$) of FeNiN6-DAC bonded with OO* *via* end-on configuration as a function of number of net electrons of system ($n - n_0$), indicates a nearly linear relationship. The blue dots and dash curve denote the DFT calculated energies and

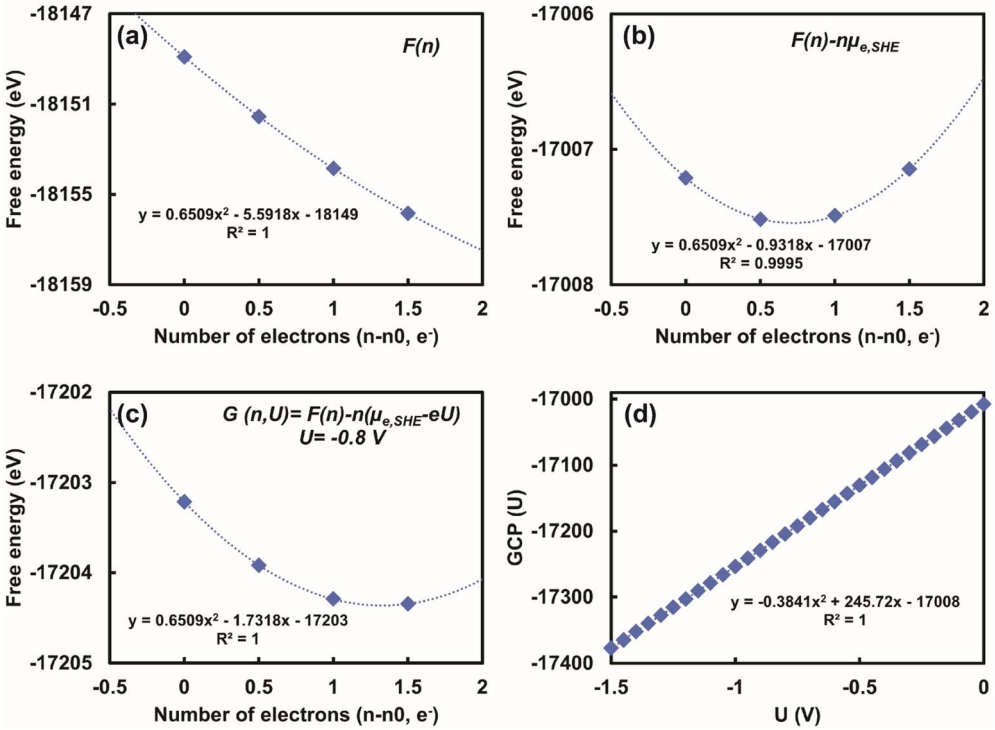

Fig. 2 Behaviour of free energy and grand canonical potential as a function of the number of electrons. (a) The free energies of OO* bonded to FeNiN6-DAC a function of number of electrons ($n - n_0$), indicates a nearly linear relationship. (b) The relation between free energy and number of net electrons becomes quadratic when the energy contribution of each electron at SHE is subtracted from total free energy. (c) Minimization of free energy as a function of number of net electrons when an external potential is applied to the system. The free energy minimum is shifted toward higher electron numbers as U is goes to more negative values, ensuring that the reaction progresses in the forward direction. The quadratic dependence allows the optimum number of electrons and grand canonical potential GCP(U) to be predicted for each U. (d) The dependence of the grand canonical potential GCP(U) as a function of applied potential for of FeNiN6-DAC bonded to OO*. The blue dots and dash curve denote the DFT calculated energies and polynomial 2nd order fitting, respectively.

polynomial 2nd order fitting, respectively. The reported free energy ($F(n)$) contains four different parts as follows:

$$F(n) = E_{tot}(n) + E_{ZPE}(n) - E_{TS}(n) - E_{solvent}(n) \quad (12)$$

where $E_{tot}(n)$ is the total energy of the system, $E_{ZPE}(n)$ and $E_{TS}(n)$ are the zero-point energy and entropy contributions, respectively, and $E_{solvent}(n)$ is single-point solvation energy correction. $E_{tot}(n)$, $E_{TS}(n)$ and $E_{solvent}(n)$ are obtained from single point energy calculations in the jDFTx code using CANDLE solvation. The zero-point energy contribution ($E_{ZPE}(n)$) for each reaction intermediate including the three free water molecules is obtained from the vibrational frequency calculation in the VASP package along with VASPsol code to include the contributions of phonon frequency at $T = 298$ K. The zero-point energy contribution of FeNiN6-DAC as the adsorption sites is assumed to be negligible. Based on the 2nd order polynomial fit of free energy ($F(n)$) *vs.* net charges, we can calculate the differential capacitance, $C_{diff} = \frac{\partial n}{\partial U} = -\frac{1}{2 \times 0.6509}$ e/V and potential of zero charge of $U_{PZC} = 0.9318$ V. The differential capacitance indicates that the capacitance of the electrode interface decreases by 0.7682 units for each unit increase in electrode potential. Table S1† shows the fitting parameters obtained from quadratic fitting of $F(n)$ *vs.* net charge to obtain the grand canonical potential along with differential capacitance and potential of zero charge for all the reaction intermediates and their correspondence transition state.

As shown in Fig. 2b, when the energy contribution of each electron at SHE is subtracted from total free energy ($F(n) - n\mu_{e,SHE}$), the relation between free energy and number of electrons becomes quadratic with a minimum at the net charge of $n - n_0 = 0.7158$ e$^-$. In fact, this quadratic dependence leads to the optimum number of electrons for each potential. As shown in Fig. 2c, when an external potential is applied to the system, the free energy minimum is shifted toward higher electron numbers of $n - n_0 = 1.3303$ e$^-$, ensuring that the reaction progresses in the forward direction. Fig. S3a† indicates the dependence of the number of net electrons of the system as a function of applied potential, suggesting a linear relationship with R^2 value of 1 and slope of $C_{diff} = \frac{-1}{2a} = -0.7682$ e/V and intercept value of $C_{diff}U_{PZC} = 0.7158$ e. Fig. 2d displays the polynomial dependence of the grand canonical potential GCP(U) as a function of applied potential for FeNiN6-DAC bonded to OO* with R^2 value of 1 and an equation as follows:

$$\mathrm{GCP}(U) = -\frac{e^2 C_{\mathrm{diff}}}{2}U^2 + \left(n_0 + (n-n_0)_{\mathrm{at}\ \ U=0}\right)eU + \mathrm{GCP}(U=0)$$
$$= -0.3841\,U^2 + 245.7158\,U - 17\,005.4716 \qquad (13)$$

So, the reaction barrier for step ab ($OO^* \xrightarrow{H^+} OOH^*$) is shown in Fig. S3b† and can be written as:

$$G^{\ddagger}_{ab} = 0.0313\,U^2 + 0.0625\,U + 0.4543 \qquad (14)$$

As shown in Fig. 3a, to form OOH* when the OO* is chemisorbed to Fe active site *via* end-side configuration, we introduce three water molecules (H_6O_3) to the system. The proton in the H_6O_3 cluster reacts with the OO* molecule to form the OOH* intermediate while producing a cluster of 2 solvated H_2O molecules and one solvated OH ion. Four images (01–04) were inserted to search for TS, where 00 and 05 indicate the reactant and product, respectively, *via* the minimum energy path (MEP). The dashed green lines are shown to clarify the atom displacement along the reaction pathway. Fig. 3a and S4–S8† show the reaction pathway of steps ab ($OO^* \xrightarrow{H^+} OOH^*$), bc ($OOH^* \xrightarrow{H^+} O^* + H_2O$), cd ($O^* \xrightarrow{H^+} OH^*$), da ($OH^* \xrightarrow{H^+} H_2O$), ae ($^* \xrightarrow{H^+} H^*$), and ef ($H^* \xrightarrow{H^+} H_2$), indicating the optimized structures of the initial, transition, and final states at applied potential of 1 V *vs.* RHE. Fig. 3b shows the free energy barrier for the step ab ($OO^* \xrightarrow{H^+} OOH^*$) at different numbers of net electrons ($n - n_0$) in the system. This shows the maximum energy barrier of 0.5 eV and 1.4 eV at net charge of $n - n_0 = 0\ e^-$ for the conversion of $OO^* \xrightarrow{H^+} OOH^*$ in forward and backward directions, respectively, on Fe site of FeNiN6-DAC. Fig. 3c shows the O–H bond distance variation of TS 03 of step ab, indicating the increase in the bond length at more positive potentials. Based on our calculations, the transition state moves towards final state as more negative potential applied indicating the forward direction of reaction progresses.

The proton transfer from three water molecules to OOH* intermediate can go through two different pathways: (i) formation of HOOH* intermediate to produce H_2O_2 *via* a two-electron reaction pathway and (ii) formation of O* intermediate and H_2O water *via* a four-electron reaction pathway (Scheme 1). As shown in Fig. S2,† the energy level of O* is lower than the energy level of HOOH* suggesting that the four-electron reaction pathway is more favorable on FeNiN6-DAC than the two-electron reaction pathway.

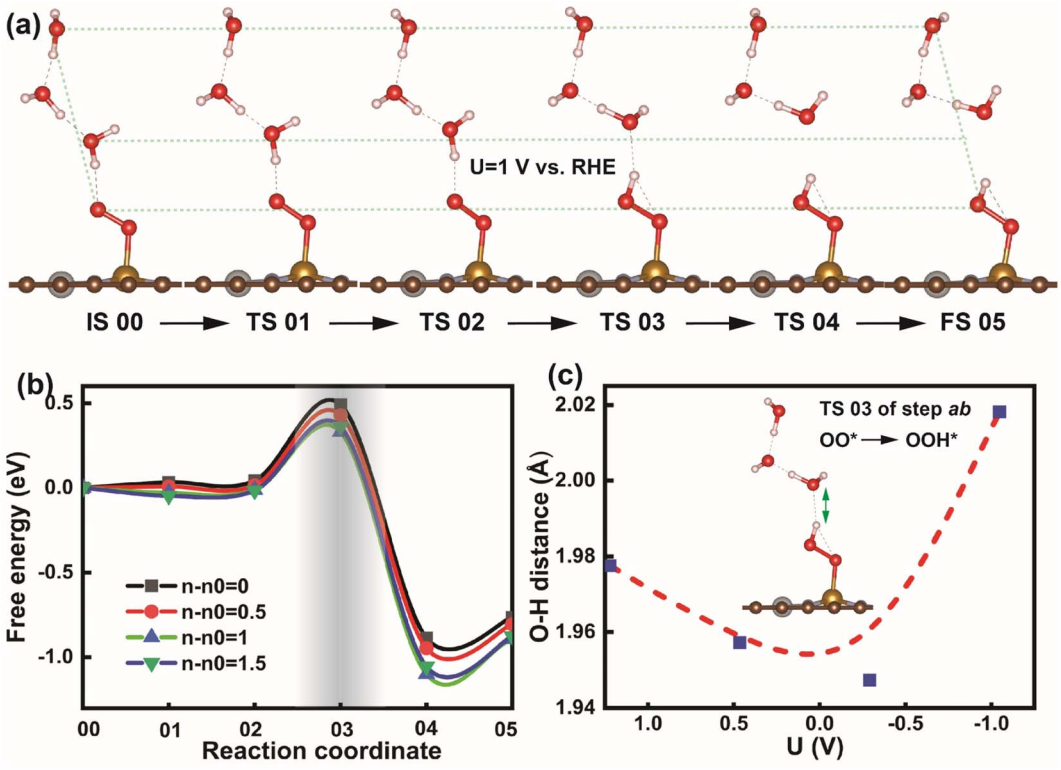

Fig. 3 Investigation of transition states of $OO^* \xrightarrow{H^+} OOH^*$. (a) Reaction pathway of step ab ($OO^* \xrightarrow{H^+} OOH^*$), indicating the optimized structures of initial, transition, and final states at the applied potential of $U = 1$ V *vs.* RHE. The transition state moves towards final state as more negative potential applied. Four images (01–04) were inserted to search for TS, and 00 and 05 indicate the reactant and product, respectively, *via* minimum energy path (MEP). The dash green lines are to show the atom displacement along the reaction pathway. (b) The free energy barrier for the step 01 ($OO^* \xrightarrow{H^+} OOH^*$) at different numbers of net electrons ($n - n_0$) in the system. It shows the maximum energy barrier of 0.5 eV and 1.4 eV at net charge of $n - n_0 = 0\ e^-$ for the forward and backward conversion of $OO^* \xrightarrow{H^+} OOH^*$, respectively, on Fe site of FeNiN6-DAC. (c) O–H bond distance variation of TS 03 of step ab *vs.* the applied potential.

In addition, we investigated the charge transfer and spin of the Fe active site. Fig. 4a and b show the charge transfer and spin of Fe along the reaction pathway of step ab ($OO^* \xrightarrow{H^+} OOH^*$) at the applied potential of 1 V *vs.* RHE. This indicates the increase in both charge transfer and spin along the proton transfer. Fig. 4c and d shows the contour plot of charge transfer and spin of system *vs.* net electrons and reaction pathway of $OO^* \xrightarrow{H^+} OOH^*$. The transition state TS 03 of step ab shows the

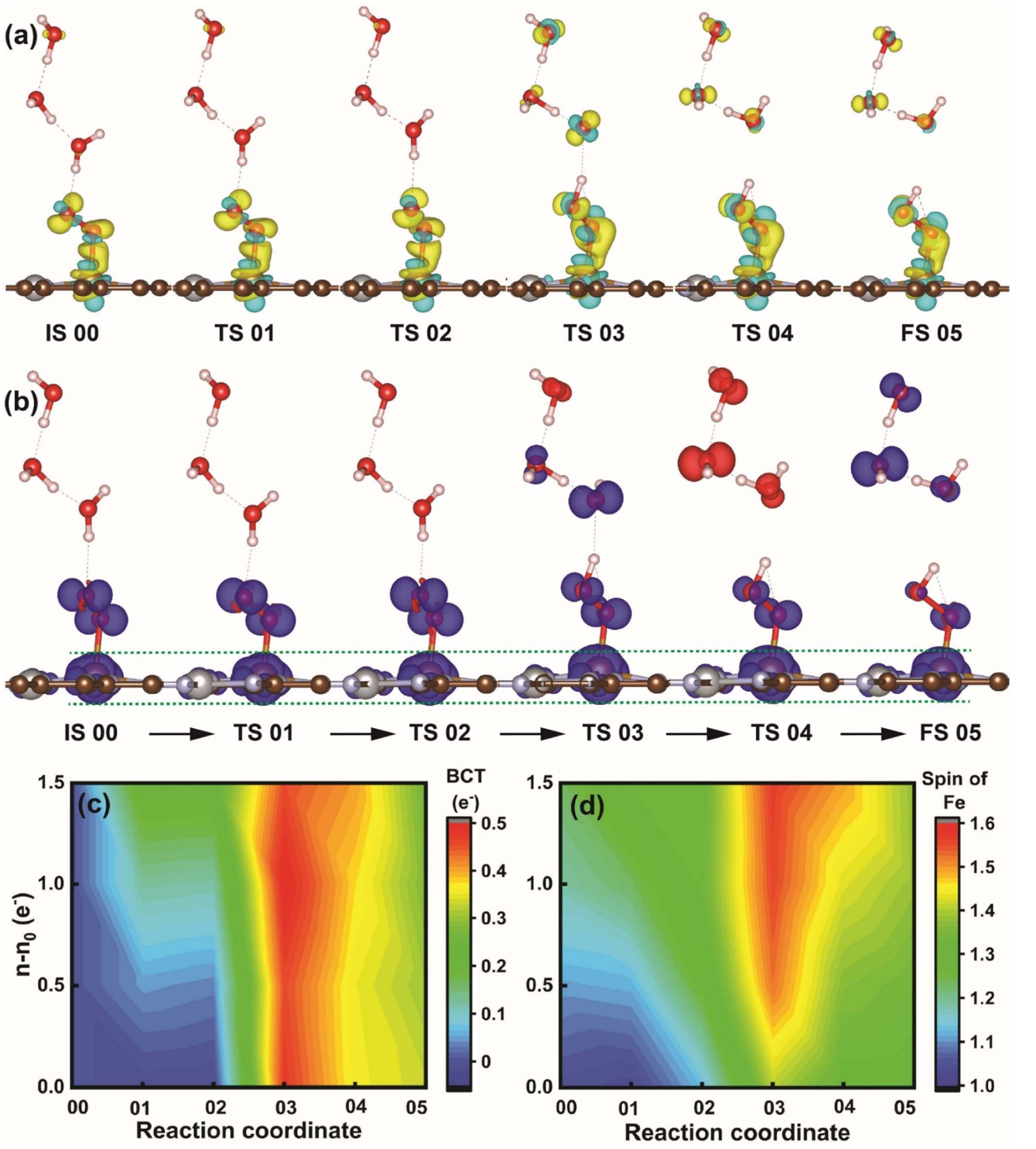

Fig. 4 Investigation of charge transfer and spin of Fe. (a) Charge transfer and (b) spin of system along the reaction pathway of step ab ($OO^* \xrightarrow{H^+} OOH^*$) at the applied potential of $U = 1$ V *vs.* RHE. This indicates the increase in both charge transfer and spin along the reaction pathway and proton transfer. The dash green lines are to show the increase in the spin of Fe atom in the *z*-axis along the reaction pathway. Contour plot of (c) charge transfer and (d) spin of system *vs.* net electrons and reaction pathway of step ab ($OO^* \xrightarrow{H^+} OOH^*$).

highest charge transfer and spin density at Fe. The charge transfer for steps bc ($OOH^* \xrightarrow{H^+} O^* + H_2O$), cd ($O^* \xrightarrow{H^+} OH^*$), and da ($OH^* \xrightarrow{H^+} H_2O$) along the reaction pathway at the applied potential of 1 V *vs.* RHE is shown in Fig. S12–S15.† This indicates the increase in charge transfer along each proton transfers.

The density of states (DOS) of Fe atom in FeNiN6-DAC system for initial and final states of step ab ($OO^* \xrightarrow{H^+} OOH^*$) is shown in Fig. 5a, indicating the presence of the $d_{x^2-y^2}$ orbital of Fe atom at the Fermi level. Fig. 5b shows the position of the d_{z^2} orbital and Fermi level along the reaction pathway of step ab ($OO^* \xrightarrow{H^+} OOH^*$), indicating that both decrease along the proton transfer with a minimum at the TS 03. Fig. 5c shows the molecular orbital of 3d orbital of free Fe and Fe during the step ab ($OO^* \xrightarrow{H^+} OOH^*$). By comparing the molecular orbital of free FeNiN6-DAC with FeNiN6-DAC bonded to OO*, we see that $d_{x^2-y^2}$ and d_{z^2} goes to lower and higher energy states, respectively, after the adsorption of OO*. This also indicates that d_{xy} orbital is empty, $d_{x^2-y^2}$ and d_{z^2} orbitals are singly occupied, and d_{xz} and d_{yz} orbitals are doubly occupied. The spin crossover can also happen during the proton transfer ($OO^* \xrightarrow{H^+} OOH^*$) where Fe goes from the triplet state to the doublet state with an empty d_{z^2}. Fig. S17 and S18† show the band structure and partial density of states (PDOS) analysis of the initial and final states of step ab $OO^* \xrightarrow{H^+} OOH^*$. In both initial and final states, there are bonding and antibonding orbitals on d_{xy}, $d_{x^2-y^2}$, and d_{z^2}. The biggest change during the proton transfer is on the d_{z^2} orbital, suggesting that this orbital participates in the hybridization.

We predict the free energy reaction barriers based on GCP(U). Fig. 6a shows the schematic representation of free energies at 298.15 K and pH of 1 and applied potentials of 1 V (blue) and 0.2 V *vs.* RHE (red). This summarizes all reaction intermediates (a–f) and transition state (TS) free energies involved in the reduction of O_2 on FeNiN6-DAC at 1 V and 0.2 V constant applied potential. In order to calculate the concentration of each intermediate on Fe active site and current density *vs.* applied potential, the following equations are taken into accounts:[41]

$$\frac{dx_a}{dt} = -(k_{ab} + k_{ae})x_a + (k_{ba} + k_{ba'})x_b + k_{da}x_d + k_{ea}x_e + k_{fa}x_f \quad (15)$$

$$\frac{dx_b}{dt} = k_{ab}x_a - (k_{ba'} + k_{ba} + k_{bc})x_b + k_{cb}x_c \quad (16)$$

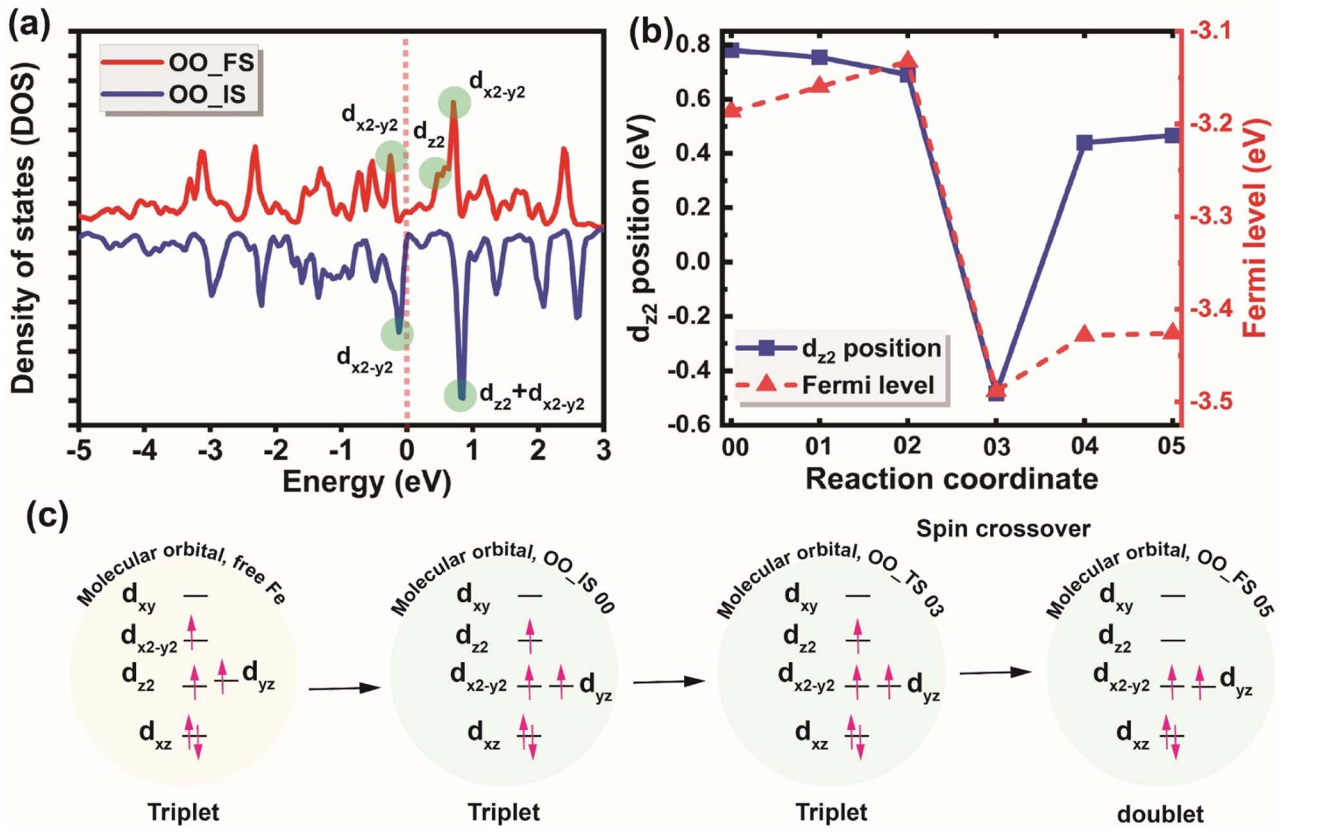

Fig. 5 Density of states analysis. (a) The density of states (DOS) of Fe atom in FeNiN6-DAC system for initial and final states of step ab ($OO^* \xrightarrow{H^+} OOH^*$), indicating the presence of $3d_{x^2-y^2}$ orbital of Fe atom on the Fermi level. (b) The position of $3d_{z^2}$ orbital and Fermi level along the reaction pathway of step ab ($OO^* \xrightarrow{H^+} OOH^*$), indicating that both reaches a minimum along the proton transfer. (c) The energy level of 3d orbitals of free Fe and Fe during the step ab, indicating that d_{xy} orbital is empty, $d_{x^2-y^2}$ and d_{z^2} orbitals are singly occupied, and d_{xz} and d_{yz} orbitals are doubly occupied.

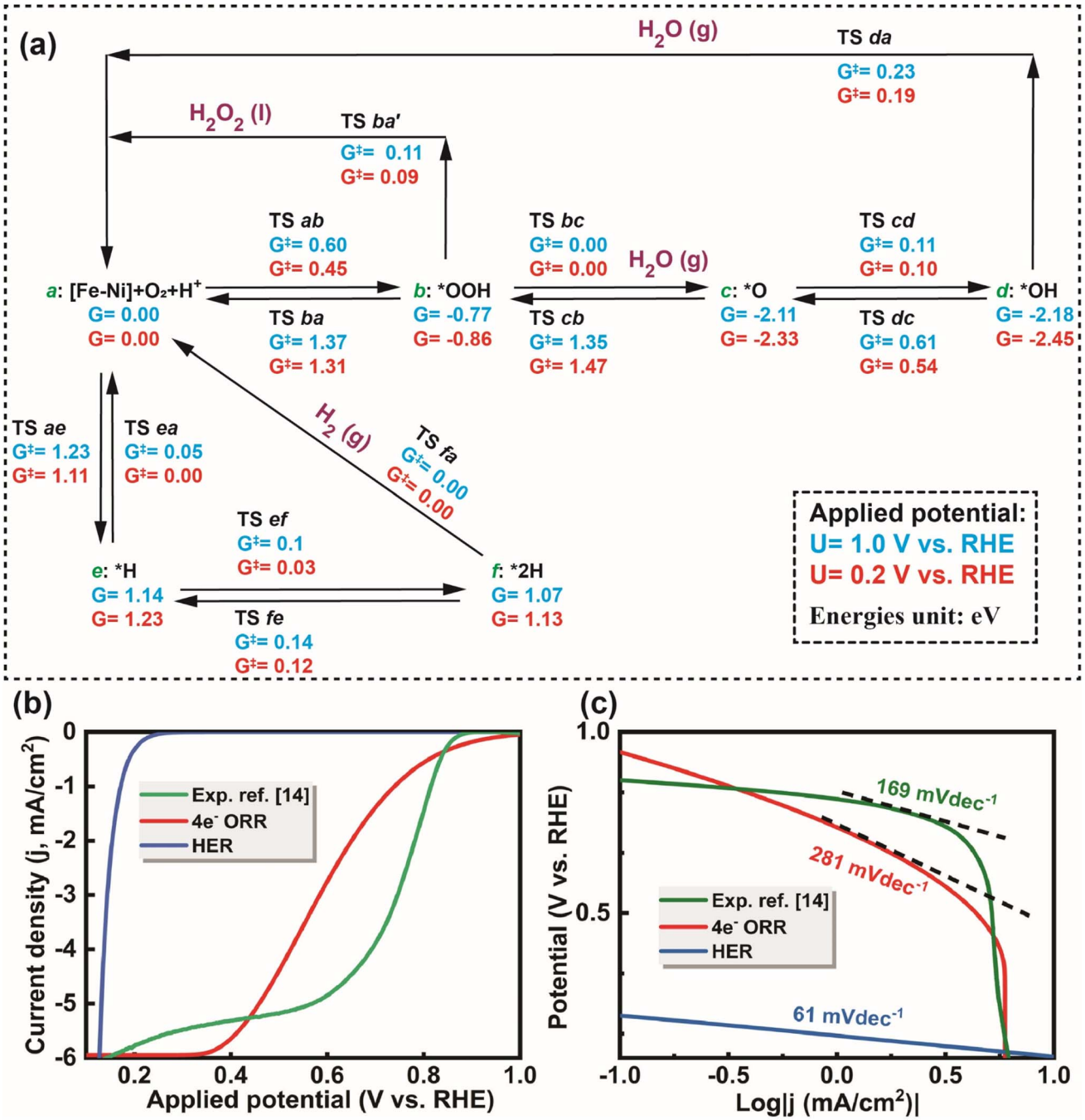

Fig. 6 QM derived free energies and predicted reaction kinetics. (a) Schematic representation of free energies at 298.15 K and pH of 1 and applied potentials of 1 V *vs.* RHE (blue) and 0.2 V *vs.* RHE (red). This summarizes all reaction intermediates (a–f) and transition state (TS) free energies involved in the reduction of O_2 on FeNiN6-DAC at applied potentials of 1 V and 0.2 V. (b) Calculated partial current densities for ORR and HER on FeNiN6-DAC along with experimental ORR data obtained from ref. 14 (green line) for comparison. (c) Theoretical Tafel slopes calculated from the *I*–*V* curves for ORR and HER on FeNiN6-DAC, showing fair agreement with the experimental ORR Tafel slope from ref. 14 (green line).

$$\frac{dx_c}{dt} = k_{bc}x_b - (k_{cb} + k_{cd})x_c + k_{dc}x_d \quad (17)$$

$$\frac{dx_d}{dt} = k_{cd}x_c - (k_{dc} + k_{da})x_d \quad (18)$$

$$\frac{dx_e}{dt} = k_{ae}x_a + k_{fe}x_f - (k_{ea} + k_{ef})x_e \quad (19)$$

$$\frac{dx_f}{dt} = k_{ef}x_e - (k_{fe} + k_{fa})x_f \quad (20)$$

where k_{ij} is the reaction rate for reaction step ij, which is calculated from the Eyring rate equation as follows:[41]

$$k_{ij}(U) = \frac{k_B T}{\hbar} \exp\left(-\frac{\Delta G_{ij}^{\ddagger}(U)}{k_B T}\right) \quad (21)$$

where $\Delta G_{ij}^{\ddagger}(U)$ is the reaction barrier for the reaction step ij, while k_B, T, and $\hbar$ are Boltzmann constant, temperature, and Planck's constant, respectively. The current density and concentrations are calculated at the steady state condition in which $\frac{dx_a}{dt} = \frac{dx_b}{dt} = \frac{dx_c}{dt} = \frac{dx_d}{dt} = \frac{dx_e}{dt} = \frac{dx_f}{dt} = 0$. The concentrations are normalized based on $\sum_{i=a}^{f} x_i = 1$.

Fig. 6b shows calculated current densities for ORR and HER on FeNiN6-DAC *vs.* applied potential along with experimental data ORR from ref. 14 (green line) for comparison. We find that the direct four-electron transfer pathway is dominant under more positive applied potentials, while the HER pathway becomes more favorable at lower applied potentials. The Tafel slope represents the rate of change of the current density with respect to the applied potential and can be used to determine and compare the kinetic parameters of the ORR reaction. Fig. 6c displays Tafel slope of 281 calculated from the *I–V* curve for ORR on FeNiN6-DAC, comparable with the experimental Tafel slope of 169 mV dec^{-1} for ORR from ref. 14 (green line). The discrepancy between the Tafel slope obtained from computational calculations and experimental results might be due to the sluggish kinetics of ORR. In addition, other possible reasons for this discrepancy can be due to the limitations on the DFT calculations such as the pseudopotential and number of explicit waters. Therefore, the agreement between the DFT- and experimental-obtained Tafel slopes might be improved by using a more accurate pseudopotential than PBE and considering more explicit waters in several directions to consider the accurate dynamic hydrogen transfer towards more accurate reaction barriers and reaction kinetics.[36] Fig. 6c displays also the Tafel slope of 61 mV dec^{-1} calculated from the *I–V* curves for HER on FeNiN6-DAC. This Tafel slope is comparable with the experimental HER Tafel slope of 129 mV dec^{-1}, shown in Fig. S19,† for Fe single atom catalyst (FeN4-SAC) from ref. 42. Fig. 7 shows the change in the concentration of ORR reaction intermediates on the Fe active site of FeNiN6-DAC at different potentials indicating the dominant coverage of surface with OH* intermediate at higher potentials. This shows that at higher potentials, the desorption of OH* intermediate to produce H_2O is the rate limiting step, while the proton transfer to O* to produce OH* intermediate is the rate limiting step at low potentials, in agreement with previous reports.[26]

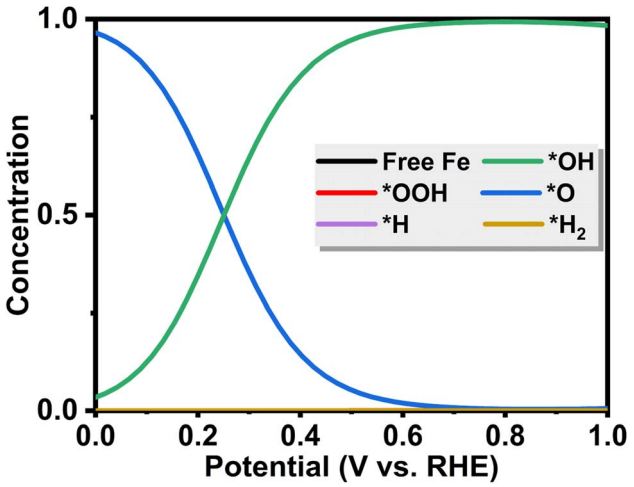

Fig. 7 Concentration of ORR intermediates. The change in the concentration of ORR reaction intermediates on the Fe active site of FeNiN6-DAC at different potentials, indicating the dominant coverage of surface with OH* intermediate at higher potentials.

4. Conclusion

In this paper, we employed grand canonical potential kinetics (GCP-K) to study the reaction mechanism and kinetics for ORR through the associative pathway and its competitive hydrogen evolution reaction (HER) on the iron–nickel dual atom catalyst (FeNiN6-DAC). The behavior of the free energy and grand canonical potential is investigated using CANDLE solvation in joint DFT calculations for reaction intermediates (OO*, OOH*, O*, OH*, and H*) and their corresponding transition states at constant potentials. Investigation of the OO* $\xrightarrow{H^+}$ OOH* step, reveals that the charge transfer and spin density of Fe reaches a maximum during the proton transfer. The ORR Tafel slope of 281 mV dec^{-1} was calculated from the *I–V* curves for ORR, comparable with the experimental Tafel slope of 169 mV dec^{-1}. The change in the concentration of ORR reaction intermediates on the Fe active site of FeNiN6-DAC at various potentials indicates that OH* and O* are the dominant intermediates at potentials >0.25 V and <0.25 V *vs.* RHE, respectively. Our study aimed to provide insights into the fundamental aspects of ORR on DACs and to guide the design of more efficient ORR catalysts.

Author contributions

Mohsen Tamtaji: conceptualization, DFT calculations, and writing. Yuyin Li: conceptualization and analysis. Yuting Cai: conceptualization and analysis. Hongwei Liu: conceptualization and writing. William A. Goddard III: supervision, conceptualization, and editing GuanHua Chen: supervision, conceptualization, and editing.

Conflicts of interest

The authors respectfully declare that there are no conflicts of interest to acknowledge for this research.

Acknowledgements

GHC acknowledges financial supports by the General Research Fund (Grant No. 17309620) and Hong Kong Quantum AI Lab, AIR@InnoHK of the Hong Kong Government. WAG thanks AIR@InnoHK and the US National Science Foundation (CBET-231117) for support.

References

1 X. Li and Z. Xiang, Identifying the impact of the covalent-bonded carbon matrix to FeN4 sites for acidic oxygen

reduction, *Nat. Commun.*, 2022, **13**(1), 57, DOI: **10.1038/s41467-021-27735-1**.

2 Z. Xu, G. Chen, F. Yang, J. Jang, G. Liu, F. Xiao, Y. Sun, X. Qiu, W. Chen, D. Su, M. Gu and M. Shao, Graphene-supported Fe/Ni single atoms and FeNi alloy nanoparticles as bifunctional oxygen electrocatalysts for rechargeable zinc-air batteries, *Electrochim. Acta*, 2023, **458**, 142549, DOI: **10.1016/j.electacta.2023.142549**.

3 H. A. Hansen, V. Viswanathan and J. K. NØrskov, Unifying kinetic and thermodynamic analysis of 2 e- and 4 e - reduction of oxygen on metal surfaces, *J. Phys. Chem. C*, 2014, **118**, 6706–6718, DOI: **10.1021/jp4100608**.

4 J. Zhang, A. Yu and C. Sun, Computational Exploration of Dual Atom Catalysts Loaded on Defective Graphene for Oxygen Reduction Reaction, *Appl. Surf. Sci.*, 2022, 154534, DOI: **10.1016/j.apsusc.2022.154534**.

5 F. Xiao, Q. Wang, G. L. Xu, X. Qin, I. Hwang, C. J. Sun, M. Liu, W. Hua, H. wen Wu, S. Zhu, J. C. Li, J. G. Wang, Y. Zhu, D. Wu, Z. Wei, M. Gu, K. Amine and M. Shao, Atomically dispersed Pt and Fe sites and Pt–Fe nanoparticles for durable proton exchange membrane fuel cells, *Nat. Catal.*, 2022, **5**, 503–512, DOI: **10.1038/s41929-022-00796-1**.

6 H. Xu, D. Cheng, D. Cao and X. C. Zeng, A universal principle for a rational design of single-atom electrocatalysts, *Nat. Catal.*, 2018, **1**, 339–348, DOI: **10.1038/s41929-018-0063-z**.

7 W. Fang, Y. Wu, S. Xin, Y. Hu, J. Dang, M. Li, B. Chen, H. Zhao and Z. Li, Fe and Mo dual-site single-atom catalysts for high-efficiency wide-pH hydrogen evolution and alkaline overall water splitting, *Chem. Eng. J.*, 2023, **468**, 143605, DOI: **10.1016/j.cej.2023.143605**.

8 F. Rehman, S. Kwon, C. B. Musgrave, M. Tamtaji, W. A. Goddard III and Z. Luo, High-throughput screening to predict highly active dual-atom catalysts for electrocatalytic reduction of nitrate to ammonia, *Nano Energy*, 2022, **103**, 107866, DOI: **10.1016/j.nanoen.2022.107866**.

9 J. Shan, C. Ye, Y. Jiang, M. Jaroniec, Y. Zheng and S. Z. Qiao, Metal-metal interactions in correlated single-atom catalysts, *Sci. Adv.*, 2022, **8**(17), eabo0762, DOI: **10.1126/sciadv.abo0762**.

10 J. Wang, C. X. Zhao, J. N. Liu, Y. W. Song, J. Q. Huang and B. Q. Li, Dual-atom catalysts for oxygen electrocatalysis, *Nano Energy*, 2022, **104**, 107927, DOI: **10.1016/j.nanoen.2022.107927**.

11 F. Kong, M. Wang, Y. Huang, G. Meng, M. Chen, H. Tian, Y. Chen, C. Chen, Z. Chang, X. Cui and J. Shi, Cu-N-bridged Fe-3d electron state regulations for boosted oxygen reduction in flexible battery and PEMFC, *Energy Storage Mater.*, 2023, **54**, 533–542, DOI: **10.1016/j.ensm.2022.11.003**.

12 Z. Chen, X. Su, J. Ding, N. Yang, W. Zuo, Q. He, Z. Wei, Q. Zhang, J. Huang and Y. Zhai, Boosting oxygen reduction reaction with Fe and Se dual-atom sites supported by nitrogen-doped porous carbon, *Appl. Catal., B*, 2022, **308**, 121206, DOI: **10.1016/j.apcatb.2022.121206**.

13 Q. Xue, Y. Wang, M. Jiang, R. Cheng, K. Li, T. Zhao and C. Fu, Engineering Electronic Spin State of a CoNi Alloy for an Efficient Oxygen Reduction Reaction, *ACS Appl. Energy Mater.*, 2023, **6**(3), 1888–1896, DOI: **10.1021/acsaem.2c03831**.

14 M. Tamtaji, Q. Peng, T. Liu, X. Zhao, Z. Xu, P. Ryan, D. Hossain, Z. Liu, H. Wong, H. Liu, K. Amine, Y. Zhu, W. A. Goddard III, W. Wu and Z. Luo, Non-bonding interaction of dual atom catalysts for enhanced oxygen reduction reaction, *Nano Energy*, 2023, **108**, 108218, DOI: **10.1016/j.nanoen.2023.108218**.

15 Y. Yan, X. Zheng, X. Li, Y. Yao and Y. Liu, Vibronic Coupling of Adjacent Single-Atom Co and Zn Sites for Bifunctional Electrocatalysis of Oxygen Reduction and Evolution Reactions, *J. Phys. Chem. Lett.*, 2022, **13**, 2548–2554, DOI: **10.1021/acs.jpclett.2c00209**.

16 J. Du, G. Han, W. Zhang, L. Li, Y. Yan, Y. Shi, X. Zhang, L. Geng, Z. Wang, Y. Xiong, G. Yin and C. Du, CoIn dual-atom catalyst for hydrogen peroxide production via oxygen reduction reaction in acid, *Nat. Commun.*, 2023, **14**, 4766, DOI: **10.1038/s41467-023-40467-8**.

17 W. Liu, L. Ding, M. Liu, X. Wang, Z. Zhang, T. Jiang, S. Huo and W.-B. Cai, Unraveling the interfacial effect of PdBi bimetallic catalysts on promoting CO2 electroreduction to formate, *Nano Res.*, 2023, **16**, 10822–10831.

18 X. Han, X. Ling, D. Yu, D. Xie, L. Li, S. Peng, C. Zhong, N. Zhao, Y. Deng and W. Hu, Atomically Dispersed Binary Co-Ni Sites in Nitrogen-Doped Hollow Carbon Nanocubes for Reversible Oxygen Reduction and Evolution, *Adv. Mater.*, 2019, **31**(49), 1905622, DOI: **10.1002/adma.201905622**.

19 Y. Cheng, S. He, J. P. Veder, R. De Marco, S. z. Yang and S. P. Jiang, Atomically Dispersed Bimetallic FeNi Catalysts as Highly Efficient Bifunctional Catalysts for Reversible Oxygen Evolution and Oxygen Reduction Reactions, *ChemElectroChem*, 2019, **6**, 3478–3487, DOI: **10.1002/celc.201900483**.

20 Q. An, J. Jiang, W. Cheng, H. Su, Y. Jiang and Q. Liu, Recent Advances in Dual-Atom Site Catalysts for Efficient Oxygen and Carbon Dioxide Electrocatalysis, *Small Methods*, 2022, **6**, 1–19, DOI: **10.1002/smtd.202200408**.

21 L. Sun, V. Reddu and X. Wang, Multi-atom cluster catalysts for efficient electrocatalysis, *Chem. Soc. Rev.*, 2022, 8923–8956, DOI: **10.1039/d2cs00233g**.

22 L. Jiao, J. Zhu, Y. Zhang, W. Yang, S. Zhou, A. Li, C. Xie, X. Zheng, W. Zhou, S. Yu and H. Jiang, Non-Bonding Interaction of Neighboring Fe and Ni Single-Atom Pairs on MOF-Derived N-Doped Carbon for Enhanced CO2 Electroreduction, *J. Am. Chem. Soc.*, 2021, **143**(46), 19417–19424, DOI: **10.1021/jacs.1c08050**.

23 R. Cepitis, N. Kongi, J. Rossmeisl and V. Ivaništšev, Surface Curvature Effect on Dual-Atom Site Oxygen Electrocatalysis, *ACS Energy Lett.*, 2023, **8**, 1330–1335, DOI: **10.1021/acsenergylett.3c00068**.

24 L. Bai, C. S. Hsu, D. T. L. Alexander, H. M. Chen and X. Hu, Double-atom catalysts as a molecular platform for heterogeneous oxygen evolution electrocatalysis, *Nat. Energy*, 2021, **6**, 1054–1066, DOI: **10.1038/s41560-021-00925-3**.

25 G. Yang, J. Zhu, P. Yuan, Y. Hu, G. Qu, B. A. Lu, X. Xue, H. Yin, W. Cheng, J. Cheng, W. Xu, J. Li, J. Hu, S. Mu and J. N. Zhang, Regulating Fe-spin state by atomically dispersed Mn-N in Fe-N-C catalysts with high oxygen reduction activity, *Nat. Commun.*, 2021, **12**, 4–13, DOI: 10.1038/s41467-021-21919-5.

26 T. Liu, Y. Wang and Y. Li, How pH Affects the Oxygen Reduction Reactivity of Fe-N-C Materials, *ACS Catal.*, 2023, **13**, 1717–1725, DOI: 10.1021/acscatal.2c05540.

27 Z. Xiao, P. Sun, Z. Qiao, K. Qiao, H. Xu, S. Wang and D. Cao, Atomically dispersed Fe-Cu dual-site catalysts synergistically boosting oxygen reduction for hydrogen fuel cells, *Chem. Eng. J.*, 2022, **446**, 137112, DOI: 10.1016/j.cej.2022.137112.

28 K. Khan, X. Yan, Q. Yu, S. H. Bae, J. J. White, J. Liu, T. Liu, C. Sun, J. Kim, H. M. Cheng, Y. Wang, B. Liu, K. Amine, X. Pan and Z. Luo, Stone-Wales defect-rich carbon-supported dual-metal single atom sites for Zn-air batteries, *Nano Energy*, 2021, **90**, 106488, DOI: 10.1016/j.nanoen.2021.106488.

29 C. Fu, X. Qi, L. Zhao, T. Yang, Q. Xue, Z. Zhu, P. Xiong, J. Jiang, X. An, H. Chen, J. S. Chen, A. Cabot and R. Wu, Synergistic cooperation between atomically dispersed Zn and Fe on porous nitrogen-doped carbon for boosting oxygen reduction reaction, *Appl. Catal., B*, 2023, **335**, 122875, DOI: 10.1016/j.apcatb.2023.122875.

30 W. Yang, Z. Jia, B. Zhou, L. Wei, Z. Gao and H. Li, Surface states of dual-atom catalysts should be considered for analysis of electrocatalytic activity, *Commun. Chem.*, 2023, **6**, 1–7, DOI: 10.1038/s42004-022-00810-4.

31 C. D. Taylor and M. Neurock, Theoretical insights into the structure and reactivity of the aqueous/metal interface, *Curr. Opin. Solid State Mater. Sci.*, 2005, **9**, 49–65, DOI: 10.1016/j.cossms.2006.03.007.

32 F. Rehman, S. Kwon, M. D. Hossain, C. B. Musgrave, W. A. Goddard III and Z. Luo, Reaction mechanism and kinetics for N2 reduction to ammonia on the Fe-Ru based dual-atom catalyst, *J. Mater. Chem. A*, 2022, **461**, 23323–23331, DOI: 10.1039/d2ta06826e.

33 M. D. Hossain, Y. Huang, T. H. Yu, W. A. Goddard III and Z. Luo, Reaction mechanism and kinetics for CO2 reduction on nickel single atom catalysts from quantum mechanics, *Nat. Commun.*, 2020, **11**, 1–14, DOI: 10.1038/s41467-020-16119-6.

34 F. Li, H. Wen and Q. Tang, Reaction mechanism and kinetics for carbon dioxide reduction on iron-nickel Bi-atom catalysts, *J. Mater. Chem. A*, 2022, **10**, 13266–13277, DOI: 10.1039/d2ta02931f.

35 M. D. Hossain, Z. Liu, H. Liu, A. Tyagi, F. Rehman, J. Li, M. Amjadian, Y. Cai, W. A. Goddard III and Z. Luo, The kinetics and potential dependence of the hydrogen evolution reaction optimized for the basal-plane Te vacancy site of MoTe2, *Chem Catal.*, 2023, **3**, 100489, DOI: 10.1016/j.checat.2022.100489.

36 C. Liu, J. Qian, Y. Ye, H. Zhou, C. J. Sun, C. Sheehan, Z. Zhang, G. Wan, Y. S. Liu, J. Guo, S. Li, H. Shin, S. Hwang, T. B. Gunnoe, W. A. Goddard III and S. Zhang, Oxygen evolution reaction over catalytic single-site Co in a well-defined brookite TiO2 nanorod surface, *Nat. Catal.*, 2021, **4**, 36–45, DOI: 10.1038/s41929-020-00550-5.

37 M. Tamtaji, S. Cai, W. Wu, T. Liu, Z. Li, H. Y. Chang, P. R. Galligan, S. I. Iida, X. Li, F. Rehman, K. Amine, W. A. Goddard III and Z. Luo, Single and dual metal atom catalysts for enhanced singlet oxygen generation and oxygen reduction reaction, *J. Mater. Chem. A*, 2023, **11**(14), 7513–7525, DOI: 10.1039/d2ta08240c.

38 J. Song, S. Kwon, M. D. Hossain, S. Chen, Z. Li and W. A. Goddard III, Reaction Mechanism and Strategy for Optimizing the Hydrogen Evolution Reaction on Single-Layer 1T′ WSe2and WTe2Based on Grand Canonical Potential Kinetics, *ACS Appl. Mater. Interfaces*, 2021, **13**, 55611–55620, DOI: 10.1021/acsami.1c14234.

39 Y. Huang, R. J. Nielsen and W. A. Goddard III, Reaction Mechanism for the Hydrogen Evolution Reaction on the Basal Plane Sulfur Vacancy Site of MoS 2 Using Grand Canonical Potential Kinetics, *J. Am. Chem. Soc.*, 2018, **140**, 16773–16782, DOI: 10.1021/jacs.8b10016.

40 M. Tamtaji, S. Chen, Z. Hu, W. A. III and G. Chen, A Surrogate Machine Learning Model for the Design of Single-Atom Catalyst on Carbon and Porphyrin Supports towards Electrochemistry, *J. Phys. Chem. C*, 2023, **127**(21), 9992–10000, DOI: 10.1021/acs.jpcc.3c00765.

41 Y. Wang, Y. Li and T. Heine, PtTe Monolayer: Two-Dimensional Electrocatalyst with High Basal Plane Activity toward Oxygen Reduction Reaction, *J. Am. Chem. Soc.*, 2018, **140**, 12732–12735, DOI: 10.1021/jacs.8b08682.

42 K. Khan, T. Liu, M. Arif, X. Yan, M. D. Hossain, F. Rehman, S. Zhou, J. Yang, C. Sun, S. H. Bae, J. Kim, K. Amine, X. Pan and Z. Luo, Laser-Irradiated Holey Graphene-Supported Single-Atom Catalyst towards Hydrogen Evolution and Oxygen Reduction, *Adv. Energy Mater.*, 2021, **11**, 2101619, DOI: 10.1002/aenm.202101619.